Journal of
Materials Chemistry A

Materials for energy and sustainability

Accepted Manuscript

This article can be cited before page numbers have been issued, to do this please use: M. Lim, Z. Ma, D. Gunawan, Y. Y. Chng, W. Zhong, P. Ramadhany, K. Menon, D. Ruan, P. V. Kumar, A. R. Jalili, R. Amal, R. Daiyan and E. C. Lovell, *J. Mater. Chem. A*, 2026, DOI: 10.1039/D5TA09764A.

ROYAL SOCIETY OF CHEMISTRY

rsc.li/materials-a

View Article Online
DOI: 10.1039/D5TA09764A

ARTICLE

Electrochemical reduction conditioning modified Fe-based catalysts with structural disorders for efficient ammonium production from nitrite reduction

Received 00th January 20xx,
Accepted 00th January 20xx

DOI: 10.1039/x0xx00000x

Maggie Lim,[a] Zhipeng Ma,[a] Denny Gunawan,[a] Ying Ying Ch'ng,[a] Wenyu Zhong,[a] Putri Ramadhany,[a] Karan Menon,[a] Daqian Ruan,[a] Priyank Kumar,[a] Ali R. Jalili,[b] Rose Amal,[a] Rahman Daiyan,*[c] Emma C Lovell*[a]

Electrochemical reduction of NO_2^- to NH_4^+ offers a direct, energy-efficient pathway for sustainable ammonia production by circumventing the rate-determining NO_3^--to-NO_2^- conversion that constrains traditional NO_3^- reduction (NO_3RR). Herein, we introduce an electrochemical reduction conditioning (ERC) strategy to control Fe_2O_3 at different reduction potentials, generating a series of catalysts with tunable $Fe^{3+}/Fe^{2+}/Fe$ components and lattice strain. Comprehensive *ex situ* and *in situ* characterizations reveal that more negative ERC potentials induce greater structural disorder (i.e., tuned $Fe/FeO/Fe_2O_3$ components and pronounced lattice strain) which collectively enhance NO_2^- adsorption, water dissociation and hydrogenation of intermediates while suppressing competing H_2 evolution. Theoretical calculations support that these defective catalyst surface lower the energy barriers for NO_2^- adsorption. As a result, the optimized ERC-treated Fe_2O_3 catalyst achieves a high NH_4^+ production rate of 153 nmol s^{-1} cm^{-2}, Faradaic efficiency of 93% and partial current density of ~ 96.5 mA cm^{-2} at -1.0 V vs RHE. Integration with plasma-generated NO_2^--rich electrolytes further demonstrates stable, decentralized NH_4^+ production, yielding 32 nmol s^{-1} cm^{-2}. This work clarifies the mechanistic role of ERC-induced structural disorders in NO_2RR and provides design principles for next-generation metal-oxide catalysts enabling sustainable nitrogen-cycle management.

1 Introduction

Ammonia (NH_3), one the world's most produced chemicals, was produced at a scale of 200.7 million tonnes in 2024 and is projected to grow by ~ 5% over the next decade.[1,2] It underpins global food security through its dominant use in fertilizers and also serves as a key feedstock for various manufacturing sectors, including pharmaceuticals, plastics, and textiles.[3–6] Recently, NH_3 has also attracted interest as a hydrogen carrier because it has a higher energy density (33.5 kWh L^{-1} liquid NH_3) than gaseous hydrogen (2.4 kWh L^{-1} H_2),[3,7] offering a more efficient way to store and transport hydrogen.[6] It also benefits from its existing, well-developed global production, storage, and transport infrastructure,[6,8] making it central to the emerging global hydrogen economy and Power-to-X pathways.[8] However, over 96% of NH_3 is still made via the century-old Haber-Bosch (HB) process,[9] which reacts nitrogen and hydrogen gases under extreme conditions, ranging from 400 to 650 °C and from 150 to 200 bar.[10] The hydrogen used in this process is primarily derived from steam methane reforming, an energy-intensive process that consumes significant amounts of fossil fuels.[11,12] The HB process is estimated to consume ~ 1% to 2% of the world's total energy and contribute to substantial greenhouse gas emissions of ~ 1.5% of global carbon dioxide emissions.[11,12] While the HB process has been instrumental in increasing agricultural yields by enabling mass production of NH_3, it is economically feasible only on a large, centralized scale.[9,13] This dependence on large-scale, fossil-based production conflicts with the envisioned role of NH_3 in a low-carbon economy and its potential as a renewable energy carrier for hydrogen, highlighting the urgent need for scalable, decentralized, and renewable-powered alternatives to produce "green" NH_3.

The electrochemical conversion of NO_x species (i.e., NO_3^- and NO_2^-) to NH_3/NH_4^+ using renewable energy has emerged as a promising green alternative to conventional NH_3 synthesis. The NO_x reduction reaction (NO_xRR) can achieve higher NH_3 yield and Faradaic efficiency than other proposed green ammonia production methods, such as the direct N_2 electroreduction reaction (eNRR), which suffers from sluggish kinetics and low selectivity due to the strong N≡N bond in N_2.[14–17] Another proposed method, Li-mediated N_2 reduction (Li-NRR), despite achieving high yield and nearly 100% Faradaic efficiency, is limited by high overpotentials, system instability and costly feedstocks (i.e., pure N_2 and H_2, as well as scarce Li metal).[6,8,18] NO_xRR also offers the benefit of closing the NO_x loop cycle by

[a] Particles and Catalysis Research Laboratories and School of Chemical Engineering, UNSW Sydney, Sydney, NSW 2052, Australia.
[b] School of Chemistry, UNSW Sydney, Sydney, NSW 2052, Australia.
[c] Particles and Catalysis Research Laboratories and School of Minerals and Energy Resources Engineering, UNSW Sydney, Sydney, NSW 2052, Australia.

Supplementary Information available: Supplementary Figures S1-S20 and supplementary Tables S1-S3. See DOI: 10.1039/x0xx00000x

View Article Online
DOI: 10.1039/D5TA07641A

valorizing pollutants from sources such as power plants, industries and agriculture, producing NH_3 under mild conditions and thereby contributing to pollution reduction and resource recycling.[8] Moreover, NO_x can be synthesized from atmospheric nitrogen using plasma technology,[6,19–21] and when combined with the NO_xRR process, this presents the potential for a self-sustaining, decentralized, green NH_3 production system powered entirely by renewable energy sources.[6]

Among the NO_xRR pathway, the NO_3^- reduction reaction (NO_3RR) to NH_3/NH_4^+ is an eight-electron, multi-step process in which the initial adsorption and deoxygenation of NO_3^- to NO_2^- has been reported to involve a high-energy barrier, and depending on the catalysts and reaction conditions, may constitute the rate-determining step (RDS).[22–24] These limitations, combined with the relatively weak binding energy of nitrate and nucleophilicity compared with nitrite when interacting with transition metals,[25–28] restrict NO_3RR efficiency. A promising route to improve the viability of NH_3/NH_4^+ production is to start directly from NO_2^-, which bypasses one of the most energetically demanding step, requires fewer electrons, thus offering a more direct and energy-efficient pathway to NH_3. Achieving this goal requires careful control of the NO_x feedstocks. Plasma technology facilitates this by enabling precise control over the relative production of NO_2^- and/or NO_3^- species in solution, thereby providing a pathway to leverage NO_2^- reduction reaction (NO_2RR) directly. Recent studies have explored the optimization of plasma parameters, such as reactor design, discharge power, operational modes, and plasma activation duration, to enhance NO_x yields and fine-tune the NO_2^-/NO_3^- ratios in plasma-activated solutions.[6,21] However, the impact of variations in reaction medium solution conditions (e.g., pH or ion types) on final NO_x yields, NO_2^-/NO_3^- ratios, and their subsequent influence on NO_xRR activity remains an area for further investigation.

Despite the advantages of NO_2RR, the factors governing its electrocatalytic activity remain unclear. In particular, catalysts that efficiently reduce NO_3^- are not always effective for NO_2^- reduction, indicating that the active sites and mechanistic requirements for NO_2RR differ from those of NO_3RR. This discrepancy arises from several factors: (1) the adsorption behaviors of NO_3^- and NO_2^- driven by differences in their distinct molecular structures and electronic configurations, where catalysts optimized for NO_3^- adsorption may not interact as effectively with NO_2^-; (2) differences in electron-proton transfer steps, as NO_3RR involves an additional electron-proton transfer step to convert NO_3^- to NO_2^-, necessitating different active sites or catalytic properties than those required for the direct reduction of NO_2^-; and (3) the specificity of surface active sites, as those effective for NO_3^- binding and reduction may not exhibit similar efficacy for NO_2^-. These factors collectively underscore the complexity in designing catalysts capable of efficiently facilitating both NO_3RR and NO_2RR, highlighting the importance of tailored strategies to optimize NO_2RR activity.

Among various transition-metal catalysts, Fe-based materials have shown considerable promise due to their cost-effectiveness and catalytic performance.[29–31] Fe_2O_3, in particular, has been extensively studied for NO_3RR, with well-characterized mechanisms and RDS. Research indicates that the key RDS for Fe_2O_3 catalysts involves the reduction of NO_3^- to NO_2^-, and that modifying Fe_2O_3 by alloying with other transition metals and inducing defects can shift the RDS toward hydrogenation processes.[29,30] These findings underscore the dynamic role of Fe species, where Fe^{3+} and Fe^{2+} facilitate electron transfer to overcome the high energy barriers in NO_3RR. However, the established catalytic efficiency of Fe_2O_3 in NO_3RR does not guarantee similar performance in NO_2RR. The NO_2RR may involve different reaction intermediates and electron transfer dynamics, potentially requiring alternative active site properties or crystal structures.[26,28,32] Consequently, the behavior of Fe_2O_3 in NO_2RR remains underexplored, representing a significant knowledge gap in understanding the role of surface chemistry and the electronic interactions that govern NO_2RR activity. Addressing this gap requires detailed investigations into the surface chemistry, electron transport mechanisms, and active site engineering of Fe_2O_3 specific to NO_2RR.

Strain engineering has emerged as a promising strategy to enhance catalytic activity by altering crystal structures, inducing lattice distortions, and optimizing active sites.[33,34] In fact, variations in electrochemical reduction conditions can introduce defects that lead to non-stoichiometry, resulting in significant structural changes and creating lattice strains in defect regions.[33,35,36] These strains can modulate the local electronic structure at the catalyst surface, thereby tuning interactions between reaction species and the catalyst.[35] While strain has been shown to enhance catalytic activity in reactions like NO_3RR,[35,37,38] its specific effects on NO_2RR performance remain poorly understood. In particular, the detailed relationship between strain-induced electronic structure changes and the resulting local physiochemical properties of NO_2RR intermediates on Fe_2O_3 catalysts is unclear. Additionally, the influence of variables such as applied potential, on the creation and maintenance of strain has not been thoroughly examined. Furthermore, the operational stability of strained catalysts is not well-documented, as mechanical relaxation or structural changes over time could diminish the benefits of strain. Therefore, mechanistic studies that correlate the degree of strain in Fe_2O_3 with its catalytic activity and selectivity in NO_2RR are essential to guide the rational design of strained Fe_2O_3 catalysts.

This study employs an electrochemical reduction conditioning (ERC) strategy to control Fe_2O_3 catalysts at different reduction potentials, producing a series of catalysts (pristine Fe_2O_3, LR-Fe_2O_3 and HR-Fe_2O_3) for investigating their activity for NO_2RR-to-NH_4^+ under alkaline conditions. This approach enables a systematic evaluation of how $Fe^{3+} \rightarrow Fe^{2+}/Fe$ reduction, with tunable $Fe/FeO/Fe_2O_3$ components and strain induction, influences NO_2RR performance. Through a suite of *ex situ* and *in situ* characterization techniques, it is revealed that more negative ERC potentials induced greater structural disorder (i.e., tuned $Fe/FeO/Fe_2O_3$ components and lattice strain), thereby enhancing NO_2^- adsorption, promoting hydrogenation of intermediates and suppressing competing H_2 evolution. Density functional theory (DFT) calculations on the pristine and

View Article Online
DOI: 10.1039/D5TA09764A

defective hematite surfaces provide further corroboration of these findings. Specifically, the structural defects induced by electrochemical reduction act as bifunctional active sites that simultaneously enhance NO_2^- binding and activate water dissociation to provide the surface protons essential for NO_2^- reduction process, offering valuable insights for designing next-generation metal-oxide catalysts. These ERC-treated catalysts are further tested in plasma-generated, optimized NO_2^--rich electrolytes obtained by tuning solution pH and plasma reactor voltage to produce NH_4^+, showcasing substantial advantages for green ammonium production through bypassing the NO_3^--to-NO_2^- step and reducing overall energy costs.

2 Results and discussion

In this work, Fe_2O_3 catalyst powders were prepared through a precipitation-calcination route. Briefly, Fe_2O_3 powders were obtained by reacting iron (III) nitrate with sodium carbonate, followed by calcination at 400 °C in flowing air. The resulting Fe_2O_3 powder was drop-cast onto carbon fibre paper to prepare the pristine Fe_2O_3 electrode. The characteristics of the Fe_2O_3 electrodes were further modified using an electrochemical reduction conditioning (ERC) strategy at different applied potentials, with the resulting electrodes denoted as eR-Fe_2O_3. Specifically, prior to electrochemical testing, the Fe_2O_3 electrodes were pre-treated at reduction potentials of -1.0 V or -2.0 V vs reversible hydrogen electrode (RHE) for 0.5 h. The Fe_2O_3 electrodes conditioned at -1.0 V are referred to as Low-Reduction Fe_2O_3 (LR- Fe_2O_3), whereas those treated at -2.0 V are designated as High-Reduction Fe_2O_3 (HR- Fe_2O_3) (**Experimental Section**).

The NO_2RR activity of pristine Fe_2O_3 and eR-Fe_2O_3 electrodes treated with different ERC potentials (i.e., LR-Fe_2O_3, and HR-Fe_2O_3) were evaluated within a two-compartment H-cell system using an electrolyte composed of 0.1 M KOH and 0.1 M KNO_2 (**Experimental Section**). Across the applied potentials from -0.4 to -1.4 V vs RHE, HR-Fe_2O_3 exhibits the highest NH_4^+ production rate and Faradaic efficiency (FE_{NH4+}), followed by LR-Fe_2O_3, and lastly, pristine Fe_2O_3 (**Figure 1a** and **1b**). Specifically, HR-Fe_2O_3 achieves its optimal NH_4^+ production performance at -1.0 V vs RHE, with a production rate and FE_{NH4+} of 154 nmol s^{-1} cm^{-2} and 93%, respectively. However, at more negative potentials beyond -1.0 V vs RHE, while the NH_4^+ production rate remains relatively high, FE_{NH4+} begins to decrease, indicating increased competition from side reactions and reduced selectivity toward NH_4^+.[39–41] The chronoamperometric *i-t* curves depicted in **Figure S1** demonstrate that HR-Fe_2O_3 maintains the highest partial current density for NH_4^+ production of ~ 90.3 mA cm^{-2} among all samples at NO_2RR applied potential of -1.0 V vs RHE. As a control, to ensure that prolonged ERC treatment does not further change the catalytic activity, Fe_2O_3 was ERC-treated for 1 h (double reduction length) instead of 0.5 h at -2.0 V vs RHE to create an HRR-Fe_2O_3 electrode, which was then tested for its NO_2RR activity under similar operating conditions. As a result, the HRR-Fe_2O_3 catalyst exhibits essentially identical performance to the HR-Fe_2O_3 electrode (**Figure S2**), showing overlapping trends in both NH_4^+ production rate and FE_{NH4+} across the applied potentials from -0.4 to 1.4 V vs RHE, with only minor differences within experimental error bars. Hence, this work adopts a 0.5 h ERC pretreatment as the optimal pretreatment condition. Further, the analysis of side products (**Figure S3**) reveals that HR-Fe_2O_3 generates the least amount of H_2 (22 nmol s^{-1} cm^{-2}), followed by LR-Fe_2O_3 (25 nmol s^{-1} cm^{-2}), with pristine Fe_2O_3 producing the most (28 nmol s^{-1} cm^{-2}). This suggests that ERC treatment helps suppressing the hydrogen evolution reaction (HER), with more negative reduction treatment potentials leading to greater suppression of HER.

Polarization curves (**Figure S4, a-c**) indicate that both LR-Fe_2O_3 and HR-Fe_2O_3 exhibit slight improvements in total current densities (*j*) compared to pristine Fe_2O_3 across tested potentials in electrolytes of 0.1 M KOH, 0.1 M KOH + 0.1 M KNO_3, and 0.1 M KOH + 0.1 M KNO_2. For instance, at -1.0 V vs RHE in 0.1 M KOH + 0.1 M KNO_2 electrolyte (**Figure S4c**), the *j* achieved by pristine Fe_2O_3 is -60.1 mA cm^{-2}, while LR-Fe_2O_3 and HR-Fe_2O_3 show improvements of ~ 16% (-69.9 mA cm^{-2}) and ~ 22% (-73.0 mA cm^{-2}), respectively. Similarly, in the electrolytes of 0.1 M KOH only (**Figure S4a**) and 0.1 M KOH + 0.1 M KNO_3 (**Figure S4b**), at -1.0 V vs RHE, HR-Fe_2O_3 achieves the highest *j* of ~ -38.2 and -70.7 mA cm^{-2}, representing improvements of ~ 15% and 13% over pristine Fe_2O_3 (-33.1 and -62.8 mA cm^{-2}, respectively). LR-Fe_2O_3 shows modest improvements of ~ 10% (~ -36.4 mA cm^{-2}) and ~ 6.8% (-67.1 mA cm^{-2}) over pristine Fe_2O_3 in the same electrolytes. These results suggest that ERC-conditioned Fe_2O_3 catalysts exhibit slightly enhanced intrinsic activity overall. However, the difference in *j* between LR-Fe_2O_3 and HR-Fe_2O_3 is minor. A more pronounced difference is observed in the partial current density for NH_4^+ production (j_{NH4+}) under the electrolyte condition of 0.1 M KOH + 0.1 M KNO_2 (**Figure 1c**). Compared to pristine Fe_2O_3, which achieves j_{NH4+} of ~ -49.1 mA cm^{-2}, LR-Fe_2O_3 and HR-Fe_2O_3 show significant improvements of ~ 24% (-61.0 mA cm^{-2}) and ~ 37% (-67.4 mA cm^{-2}), respectively. This indicates that the more negative ERC (HR) potential enhances selectivity toward NH_4^+ production, with both treated catalysts showing a marked improvement in j_{NH4+} over pristine Fe_2O_3. As a control, to compare the activity between NO_2RR and NO_3RR, pristine Fe_2O_3 and HR-Fe_2O_3 electrodes were also used to conduct electrocatalytic NO_3RR in an electrolyte containing 0.1 M KOH and 0.1 M KNO_3. The results, presented in **Figure S5**, clearly demonstrate that both electrodes produce greater NH_4^+ and FE_{NH4+} in NO_2RR than in NO_3RR, with HR-Fe_2O_3 consistently outperforming pristine Fe_2O_3 in nitrate and nitrite reduction. Specifically, for NO_2RR, HR-Fe_2O_3 achieves a peak FE_{NH4+} of 93% at -1.0 V vs RHE, with an NH_4^+ production rate of ~ 154 nmol s^{-1} cm^{-2}. This represents a 31% improvement in productivity and 15% increase in FE_{NH4+} compared to pristine Fe_2O_3 (~ 118 nmol s^{-1} cm^{-2} and 81% at -1.0 V vs RHE). For NO_3RR, HR-Fe_2O_3 also outperforms pristine Fe_2O_3, achieving an NH_4^+ production rate of ~101 nmol s^{-1} cm^{-2} at -1.0 V vs RHE, corresponding to a 5% improvement over pristine Fe_2O_3 (~ 96 nmol s^{-1} cm^{-2}). Importantly, the results indicate that the improvements in NH_4^+ production are more pronounced in NO_2RR than in NO_3RR following the ERC treatment. This suggests that the ERC-treated Fe_2O_3 catalysts are more surface-active for NO_2RR than NO_3RR,

View Article Online DOI: 10.1039/D5TA09876A

and that ERC treatment yields better performance enhancements for NO_2RR than for NO_3RR.

Electrochemical impedance spectroscopy (EIS) was employed to understand charge-transfer resistances during the NO_2RR process. The Nyquist plots (**Figure 1d**) display a single semicircle for all electrodes, indicative of the charge transfer resistance at the electrode/electrolyte interface.[42,43] Notably, the radius of the semicircle decreases as the reduction treatment potential becomes more negative. Coupled with the equivalent circuit modeling (**Figure 1d, ii**), the results reveal that HR-Fe_2O_3 exhibits a ~ 35% lower charge transfer resistance compared to pristine Fe_2O_3 (1.4 kΩ vs 2.2 kΩ), while LR-Fe_2O_3 shows a ~ 21% reduction (1.8 vs 2.2 kΩ). These results demonstrate that the electrode preconditioned at a more negative reduction potential has reduced charge transfer resistance, thereby benefiting NH_4^+ production rates and selectivity during NO_2RR.[8] Additionally, the electrochemically active surface area (ECSA) of the catalysts was determined using cyclic voltammetry and double-layer capacitance methods (CDL) (**Figures S6-7**).[44,45] The results (**Table S1**) indicate that ECSA does not exhibit a significant difference (ranging from 5.1 to 6.7 cm^2). Therefore, the changes in performance are likely influenced by other factors, such as modifications in structure and/or surface chemistry (e.g., coordination environment and defects) as a result of ERC treatment.

To investigate the surface chemistry of the catalysts and understand how NH_4^+ production performance is influenced by ERC treatments, X-ray photoelectron spectroscopy (XPS) measurements were performed on all as prepared electrodes (pristine Fe_2O_3, LR-Fe_2O_3, and HR-Fe_2O_3). **Figure 2a** presents the high-resolution Fe 2p XPS spectra, which show doublet peaks at ~ 724.1 and 710.8 eV corresponding to Fe $2p_{1/2}$ and Fe $2p_{3/2}$, respectively.[46] These are typical binding energies for Fe^{3+} indicating Fe_2O_3.[46] In addition, a satellite peak at ~ 720.0 eV, characteristic of α-Fe_2O_3,[46] is observed. Notably, a positive shift of ~ 0.4 to 0.7 eV in the Fe 2p peaks is observed for LR-Fe_2O_3 and HR-Fe_2O_3 compared to pristine Fe_2O_3, respectively, suggesting possible changes in the coordination environment and/or induction of strain following ERC.[47–50] The fitted Fe 2p spectra (**Figure S8, a-c**) demonstrate that increasing the ERC potential (more negative) results in a further reduction of Fe species. Specifically, when the electrode is preconditioned at a low reduction (LR) potential (-1.0 V vs RHE), 19.2% of Fe_2O_3 in LR-Fe_2O_3 is reduced to Fe and FeO, accounting for 2.6% and 16.6% (**Figure S8b**), respectively. At a more negative (high reduction, HR) treatment potential (-2.0 V vs RHE), HR-Fe_2O_3 experiences a slightly larger portion of Fe_2O_3 (23.5%) being reduced to Fe and FeO, comprising 2.8% and 20.7% (**Figure S8c**), respectively. The emergence of these FeO and metallic Fe on the catalyst surface shows the tuneable FeO/Fe/Fe_2O_3 components with different ERC treatment potentials, these reconstructed metal and metal oxide species likely provide complementary active sites for NO_2RR activity, as reported in prior NO_3RR studies.[29,30,51] To further understand the Fe oxidation states, *ex situ* and *in situ* X-ray absorption near-edge structure (XANES) spectra of LR-Fe_2O_3 and HR-Fe_2O_3 catalysts were evaluated (**Figure S9**). The XANES spectra were compared with the reference compound spectra (metallic Fe and Fe_2O_3). The results clearly show that the absorption edge positions and white-line intensities of both catalysts lie between those of metallic Fe and Fe_2O_3 reference, indicating that both LR-Fe_2O_3 and HR-Fe_2O_3 catalysts possessed mixed oxidation states between metallic Fe and Fe_2O_3, corroborating the results from XPS analyses. Furthermore, under experimental conditions of open-circuit potential and -1.0 V vs RHE in 0.1 M KOH with 0.1 M KNO_2 electrolyte, the *in situ* XANES spectra remain consistent with the *ex situ* observations, confirming that these mixed-valence Fe species are maintained during operation. In addition, *in situ* PD spectra (**Figure S10**) were collected at the same conditions as the *in situ* XANES to further substantiate the coexistence of Fe and Fe oxide species in LR-Fe_2O_3 and HR-Fe_2O_3. The LR-Fe_2O_3 catalyst exhibits diffraction features at 21.3, 24.8, and 35.4°, assignable to Fe (011) (#96-230-0201), Fe_2O_3 (024) (#96-210-1168), and FeO (113) (#96-900-8637) throughout the 30 min reaction, respectively, while an additional FeO (222) (#96-900-8637) reflection at 36.3° emerged during electrolysis. Similarly, the HR-Fe_2O_3 catalysts show characteristic reflections at 21.3, 31.5, 24.8, 26.7, and 35.4°, respectively, corresponding to Fe (011, 002) (#96-230-0201), Fe_2O_3 (024, 116) (#96-210-1168), and FeO (113) (#96-900-8637) under reaction conditions. The results provide further evidence for the Fe and Fe oxide phases under reaction conditions. When correlating these findings with performance tests, higher proportions of these reduced Fe and Fe oxide species in LR-Fe_2O_3 and HR-Fe_2O_3 explain their improved NH_4^+ production rates compared to pristine Fe_2O_3. The O 1s XPS spectra and corresponding curve fittings (**Figure S11, a-c**) show a clear decrease in the proportion of lattice oxygen (peak at ~ 530 eV)[46] after ERC, which is consistent with the reduction of Fe_2O_3 evidenced by Fe 2p XPS spectra. Specifically, LR-Fe_2O_3 consists of 39.7% lattice oxygen, while HR-Fe_2O_3 comprises 34.9%, both markedly lower than pristine Fe_2O_3 (55.8%). Two

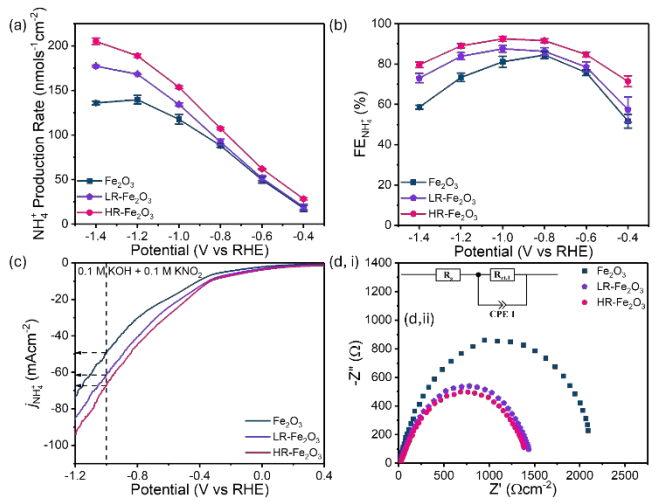

Fig. 1 NO_2RR-to-NH_4^+ production performances of Fe_2O_3, LR-Fe_2O_3, and HR-Fe_2O_3 electrodes across an applied potential range of -1.4 to -0.4 V vs RHE: **(a)** NH_4^+ production rate and **(b)** Faradaic efficiency (FE_{NH4+}). **(c)** Partial current density for NH_4^+ (j_{NH4+}) of all electrodes in 0.1 M KOH + 0.1 M KNO_2. **(d, i)** Nyquist plot and its corresponding **(d, ii)** equivalent circuit of Fe_2O_3, LR-Fe_2O_3, and HR-Fe_2O_3 electrodes.

View Article Online DOI: 10.1039/D5TA09764A

other peaks at ~ 531.0 and 532.5 eV are attributed to surface oxygen passivated with hydrogen and adsorbed oxygen (water), respectively.[52,53] The content of surface oxygen passivated with hydrogen increases from 35.4% in pristine Fe_2O_3 to 43.5% in LR-Fe_2O_3 and further to 47.5% in HR- Fe_2O_3 Similarly, adsorbed oxygen (water) increases from 8.8% in pristine Fe_2O_3 to 16.8% in LR-Fe_2O_3 and 17.6% in HR-Fe_2O_3. In fact, literature reports a direct correlation between these two oxygen species (surface oxygen passivated with hydrogen and adsorbed oxygen) and water dissociation on the catalyst surface,[54–56] suggesting that their elevated presence in ERC-treated samples increases water adsorption and subsequent dissociation. This process is crucial for supplying hydrogen during the NO_2RR, facilitating the hydrogenation of reaction intermediates and the eventual formation of NH_4^+ production (*vide infra*).

To investigate the bulk characteristics and crystal structure of the ERC-treated catalysts at different potentials, X-ray diffraction (XRD) measurements were conducted. The XRD patterns depicted in **Figure S12** and **2b** show that pristine Fe_2O_3 displays peaks at ~33.0, 35.5, 40.7, 49.4, 62.3, and 63.9°, corresponding to the (104), (110), (113), (024), (214), and (300) planes of α-Fe_2O_3, respectively (JCPDS collection code: 01-080-0597). The post-conditioned electrodes, LR-Fe_2O_3 and HR-Fe_2O_3, exhibit similar peaks, confirming the retention of the α-Fe_2O_3 structure. However, a new split from the (110) peak at ~ 35.0°, is observed to appear in both conditioned samples (**Figure 2b, ii**). This split peak, corresponding to the (101) plane of α-Fe_2O_3, indicates a partial phase shift in the crystal structure, likely caused by non-uniform distortion within the cell,[57–62] while the lacking of (101) peak in pristine Fe_2O_3 indicates the absence of this phase shift. For samples after preconditioning reduction treatments, the I_{110}/I_{101} ratio decreases with increasing (more negative) reduction potential: HR-Fe_2O_3 exhibits a lower I_{110}/I_{101} of 1.47 compared to LR-Fe_2O_3 (1.65). This trend indicates enhanced distortion and greater phase transformation at more negative reduction treatment potentials. Such cell distortion and multiphasic phenomena have been reported in the literature as results of strong lattice strains induced in the catalysts.[60,62] Furthermore, previous studies have shown that the reduction of surface species (in this work, Fe^{3+} to Fe^{2+}/Fe) can induce significant lattice strain due to localized changes in the coordination environment.[63,64] This strain, in turn, promotes the formation of multiphasic phenomena, as observed in XRD patterns in **Figure 2b, ii**. To confirm this, strain analysis using the Williamson-Hall (WH) equation was performed.[58,65] The WH plots in **Figure S13** estimate lattice strains of 6.0%, 26.3%, and 28.0% for Fe_2O_3, LR-Fe_2O_3, and HR-Fe_2O_3, respectively. Moreover, strain directly correlated with the d-band structure of the catalyst, modulating the adsorption energies of reaction intermediates.[33,34] Specifically, the increased strain can lead to the d-band center shift closer to the Fermi level,[38,66,67] which is responsible for the improved surface adsorption capabilities[4,68–71] and explains the improved water dissociation observed in HR-Fe_2O_3 and LR-Fe_2O_3 as compared to pristine Fe_2O_3 as evidenced by the XPS O 1s spectra. Furthermore, the main characteristic peaks of the catalysts, corresponding to the (104), (110) and (101) planes, were used to calculate their crystallite size (calculated via Scherrer equation) and lattice spacing, as shown in **Table S2**. The results reveal no obvious trend or significant change in crystallite size and lattice spacing with different ERC potentials. Combining XPS and XRD findings confirms that the more negative ERC potentials lead to further Fe species reduction, and thus stronger lattice strain formation, ultimately tuning the d-band center shift and leading to improved surface adsorption capabilities for protonation and NO_2^- adsorption processes.

The morphology of the Fe_2O_3, LR-Fe_2O_3, and HR-Fe_2O_3 electrodes were investigated using scanning electron (SEM) and transmission electron microscopy (TEM) (**Figure S14a** and **S14b**, respectively). The obtained SEM images of the catalysts (Fe_2O_3, LR-Fe_2O_3, and HR-Fe_2O_3) were statistically analyzed to determine the particle size distribution (**Figure S15**). Specifically, the pristine Fe_2O_3 catalyst displays nanoparticles (60 to 100 nm) that agglomerate into large clustered particles. After ERC, both LR-Fe_2O_3 and HR-Fe_2O_3 have a morphology consisting of a mixture of nanoparticles and flake-like aggregates, while LR-Fe_2O_3 shows a dominant particle size between 60 to 100 nm and HR-Fe_2O_3 shows a relatively smaller particle size range from 40 to 70 nm. The morphological changes are consistent with the structure distortion generated during the surface reconstruction. [72,73] In this study, the surface reconstruction due to lattice strain and distortion (as evidenced by the XRD measurement above) during the ECR treatment, is likely a key driver of the observed morphological changes in LR-Fe_2O_3 and HR-Fe_2O_3 electrodes. Notably, no significant change in particle size is observed, despite the catalysts being preconditioned at different reduction potentials, this is consistent with the XRD and ECSA analyses. High-resolution TEM (HR-TEM) images (**Figure 2c** and **S16**) show that all samples demonstrate lattice spacings of 0.27 and 0.25 nm corresponding to the (104) and (110) planes of α-Fe_2O_3, respectively.[46,48] Additionally, both LR-Fe_2O_3 and HR-Fe_2O_3 display a lattice spacing of 0.26 nm, which

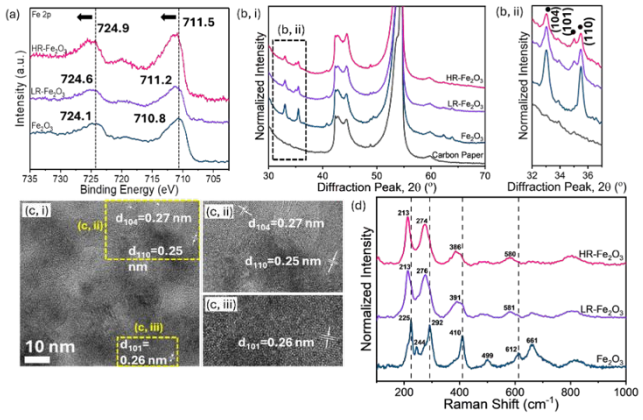

Fig. 2 (a) High-resolution Fe 2p XPS spectra of Fe_2O_3, LR-Fe_2O_3 and HR-Fe_2O_3. **(b)** Normalized XRD patterns (intensity normalized to the highest peak) of pristine Fe_2O_3, LR-Fe_2O_3, and HR-Fe_2O_3, with **(i)** and **(ii)** showing excerpts for patterns in diffraction peak range of 30° to 70° and 32° to 37°, respectively, compared with the full range (30° to 90°) patterns in **Figure S12**. **(c)** HR-TEM images of HR- Fe_2O_3 at **(i)** a magnification of 10 nm, with **(ii)** and **(iii)** showing enlarged views of specific areas indicated in **(i)**. **(d)** Normalized Raman spectra of pristine Fe_2O_3, LR-Fe_2O_3, and HR-Fe_2O_3.

View Article Online
DOI: 10.1039/D5TA09764A

corresponds to the (101) plane of α-Fe_2O_3, corroborating the dominant bulk α-Fe_2O_3 phase from XRD analyses.

To further understand the structure of the catalysts, Raman spectroscopy measurements were performed. The Raman spectra in **Figure 2d** for pristine Fe_2O_3 show seven peaks at ~ 225, 244, 292, 410, 499, 612 and 661 cm^{-1}, corresponding to α-Fe_2O_3.[74–77] For both LR-Fe_2O_3 and HR-Fe_2O_3, a negative shift in the α-Fe_2O_3 peaks is observed, with HR-Fe_2O_3 exhibiting a more pronounced shift than LR-Fe_2O_3. This negative shift in Raman wavenumbers is likely due to changes in the electronic structure, coordination environment and/or lattice effects.[78,79] Thus, the more pronounced shift observed in HR-Fe_2O_3 compared to LR-Fe_2O_3 aligns with previous characterization results, which show higher lattice strain in HR-Fe_2O_3 resulted from greater surface Fe species reduction. Besides, significant broadening of the Raman peaks observed in both LR-Fe_2O_3 and HR-Fe_2O_3 further supports the introduction of lattice strain following ERC,[57] consistent with XRD and HR-TEM characterization results. Hence, the observed negative shift and peak broadening in the Raman spectra of LR-Fe_2O_3 and HR-Fe_2O_3 can be attributed to structural disorders from non-equivalent sites in the partly reduced Fe species (Fe^{2+}/Fe) structure and/or the built strain induced within the catalysts.[57,77]. Nonetheless, it can be deduced that the Fe/FeO/Fe_2O_3 components were tuned in the post-conditioned catalysts following ERC treatment. These findings collectively indicate that more negative ERC potentials lead to greater Fe^{3+} reduction and more pronounced strain. As a result, HR-Fe_2O_3 demonstrates the best NH_4^+ production performance from NO_2RR due to its pronounced strain in the distorted structure built during the surface Fe_2O_3 reduction.

Overall, the characterization shows that ERC creates structural disorders in the catalysts by partially reducing Fe_2O_3 to FeO and/or metallic Fe, tuning Fe/FeO/Fe_2O_3 components and inducing lattice strain in the catalysts. The extent of Fe_2O_3 species reduction and strain induction increases with more negative ERC treatment potentials, with HR-Fe_2O_3 exhibiting the most pronounced of these characteristics compared to LR-Fe_2O_3 and pristine Fe_2O_3. Given that previous studies have collectively demonstrated the limited contribution of individual Fe or FeO species to enhanced NO_xRR activity,[30,51,80] the improved NO_2RR-to-NH_4^+ performance observed in this work with HR-Fe_2O_3 and LR-Fe_2O_3 is attributed to the synergistic effects of the tuned FeO/Fe/Fe_2O_3 components and lattice strain. Notably, HR-Fe_2O_3achieves the best NO_2RR activity with optimized FeO/Fe/Fe_2O_3 components and pronounced strain, delivering the most optimal NH_4^+ production rate (154 nmol s^{-1} cm^{-2}) and FE_{NH4+} (93%) at -1.0 V vs RHE.

To gain further mechanistic insight into the structural change of the active sites in the catalysts during the ERC, *in situ* Raman measurements were performed. The Raman spectra (**Figure 3a** and **3b**) reveal that the peak at ~ 408 cm^{-1}, attributed to α-Fe_2O_3,[74–77] remains until the end of the ERC treatment for all samples. However, HR-Fe_2O_3 exhibits a greater reduction in the intensity of this peak (~ 80%) compared to LR-Fe_2O_3 (~ 59%), indicating a more substantial reduction of Fe_2O_3 at more negative ERC potentials. While the low signal intensity of other α-Fe_2O_3 peaks in the HR-Fe_2O_3 spectra, likely caused by electrolyte blockage and/or high amounts of adsorbed species on the catalyst surface,[81] makes these peaks less visible, the predominant presence of Fe_2O_3 in HR-Fe_2O_3 is supported by the persistence of α-Fe_2O_3 peak at ~ 408 cm^{-1}. Throughout the ERC, both LR-Fe_2O_3 and HR-Fe_2O_3 are observed to exhibit peak shifts, peak broadening, and the emergence of new shoulder peaks (marked with black arrows in the graphs), all indicative of non-uniform strain formation in the catalysts.[57,79,82] This non-uniform strain has been reported to significantly influence catalyst performance by altering the electronic structure and shifting the d-band center closer to the Fermi level, which is a well-recognized indicator for improving the adsorption and activation abilities of the catalysts toward reaction intermediates involved in reactions.[4,33,34,68–71] Comparatively, HR-Fe_2O_3 displays these changes more prominently and earlier than LR-Fe_2O_3, suggesting a higher susceptibility to strain induction at more negative ERC potentials. This may explain why HR-Fe_2O_3 exhibits the greatest NH_4^+ production performance from NO_2RR. Unlike *ex situ* Raman and XPS analyses, *in situ* Raman spectra do not consistently show a negative shift to lower wavenumbers or the FeO peak at approximately 580 cm^{-1}. This discrepancy suggests that the FeO observed in *ex situ* analyses may not be attributed to the residual oxide after surface reduction, which is possibly attributed to the reconstructed FeO during the reoxidation when exposed to air after the reaction.[83] Thus, *in situ* Raman provides a clear view of the structural changes occurring within the catalysts at different ERC potentials. These results demonstrate that HR-Fe_2O_3, preconditioned at a more negative ERC potential, possesses more structural disorders through more obvious reduction of Fe_2O_3 into Fe^{2+}/Fe species while building lattice strain, collectively leading to enhanced NH_4^+ production performance from NO_2RR.

Further, *in situ* Fourier transform infrared (FTIR) spectroscopy measurements were conducted under electrochemical NO_2RR conditions with electrolyte (0.1 M KOH + 0.1 M KNO_2) at -1.0 V vs RHE for 15 min to probe the reaction intermediate species and elucidate the reaction pathways undertaken by these catalysts for producing NH_4^+. The *in situ* FTIR spectra, shown in **Figure 3c** and **S17**, reveal peaks corresponding to various intermediates, i.e., NH_2OH* (1215 cm^{-1}), NO_2* (1362 cm^{-1}), NH_2* (1563 cm^{-1}), NH_3* (1767 cm^{-1}), NO* (1971 cm^{-1}), NH_4* (3142 cm^{-1}), and H_2O* (3500 cm^{-1}).[44,84–92] Therefore, in agreement with the literature,[3,6,8,44] this *in situ* FTIR measurement validates the reaction mechanism for the eR-Fe_2O_3 catalysts. Specifically, the ionic NO_2^- is adsorbed onto the catalyst surface to form NO_2*, the N-O bond of which then cleave to form NO*. The formed NO* is hydrogenated subsequently to produce HNO*, H_2NO*, NH_2OH*, NH_2*, NH_3*, NH_4*, which ultimately desorbed to form NH_4^+. Moreover, it is observed that both NO_2* and NO* peaks (at ~ 1362 and 1971 cm^{-1}, respectively) exhibit a production trend in pristine Fe_2O_3, but a consumption trend in LR-Fe_2O_3 and HR-Fe_2O_3, suggesting enhanced conversion of these intermediates over the post-conditioned catalysts. When comparing LR-Fe_2O_3 and HR-Fe_2O_3, HR-Fe_2O_3 shows boosted consumption rate of NO* and NO_2*

View Article Online
DOI: 10.1039/D5TA09764A

during the *in situ* experiment, benefiting from the structure reconstruction under the more negative ERC treatment potential as discussed above. Additionally, all samples display a production trend for NH_2OH*, NH_2*, NH_3*, and NH_4* peaks. Notably, the HR-Fe_2O_3 demonstrated the most significant increase in NH_2OH* peak (at ~1215 cm^{-1}) intensity compared to pristine Fe_2O_3 and LR-Fe_2O_3. These results collectively suggest that ERC treatment promotes effective adsorption and faster consumption of NO_2RR intermediates (NO_2* and NO*), leading to improved hydrogenation pathways and ultimately higher NH_4^+ productivity. This demonstrates that the effects of ERC-induced structural disorders, i.e., optimized Fe^{3+}/Fe^{2+}/Fe components and lattice strain, collectively drive superior NO_2RR-to-NH_4^+ performance.

To gain insight into the enhanced NO_2RR performance, density functional theory (DFT) calculations were performed on pristine and defective hematite (α-Fe_2O_3) (104) surfaces. The (104) surface was selected as it represents the most prominent surface orientation in pristine hematite before ERC. Given that ERC reduces the surface oxide and introduced structural disorders, the (104) surface with oxygen vacancies was investigated to study the defective surface effects on NO_2^- adsorption and water activation processes. The calculations reveal that NO_2^- exhibits stronger adsorption on the coordinatively unsaturated Fe site adjacent to the vacancy (-

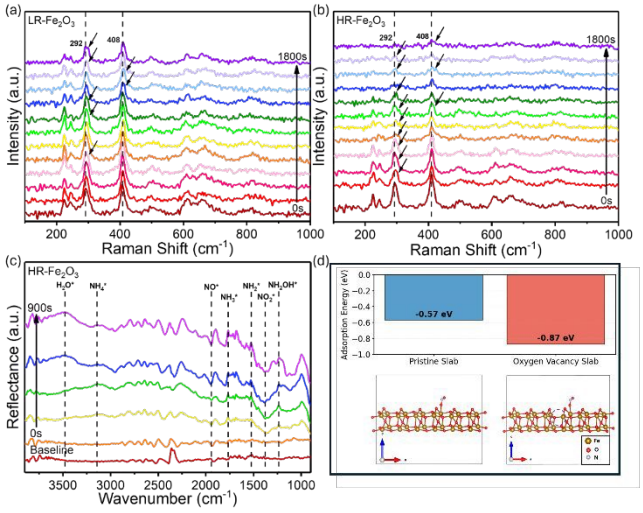

Fig. 3 *In situ* Raman spectra of **(a)** LR-Fe_2O_3 and **(b)** HR-Fe_2O_3 during 30-min ERC treatment in electrolyte condition of 0.1 M KOH + 0.1 M KNO_2. Black arrows mark the emergence of peak broadening and new shoulder peaks. **(c)** *In situ* FTIR spectra of HR-Fe_2O_3 at NO_2RR applied potential of -1.0 V vs RHE for 15 mins in electrolyte condition of 0.1 M KOH + 0.1 M KNO_2. **(d)** DFT calculations of NO_2^- adsorption energy on simulated surface representing pristine (pristine slab) and defective (oxygen vacancy slab) hematite (α-Fe_2O_3) (104) surfaces.

0.87 eV) compared to the pristine surface (-0.57 eV) (**Figure 3d**). This correlates with the experimentally observed enhanced NO_2^- conversion rates in ERC-treated catalysts. Along with enhanced nitrite binding, oxygen vacancies act as bifunctional active sites that fundamentally alter water interactions. While water dissociation on the pristine surface is thermoneutral (-0.04 eV), vacancy formation renders this process exothermic (-0.21 eV). The preferred water binding mode shifts from O-down on pristine surfaces (-1.25 eV) to a tilted configuration with hydrogen atoms oriented closer to the surface on vacancy slab (-1.55 eV), facilitating water dissociation and creating a favorable environment for proton-coupled electron transfer processes (**Figure S20**). This enhanced water activation capability ensures a steady supply of surface protons (H*) required for the improved hydrogenation steps observed in the FTIR measurements, providing molecular-level understanding of why ERC treatment enhances NO_2RR performance.

Further, NO_2RR performance of all samples (Fe_2O_3, LR-Fe_2O_3, and HR-Fe_2O_3) was evaluated over extended periods through a 15-cycle test at -1.0 V vs RHE, with each cycle comprising 0.5 h of chronoamperometry. Cycling tests were selected over continuous long-term testing to mitigate issues related to electrolyte depletion and concentration drift over time, which occur due to the consumption and gradual depletion of NO_2^- species in a batch mode setup.[8,93,94] By mimicking this through cycling test, it ensures reproducible stability evaluation and a more reliable assessment of catalyst performance under conditions closer to practical operation. As evidenced by the steady chronoamperometric *i-t* curves and stable NH_4^+ production rate shown in **Figure S18**, all electrodes demonstrate high NO_2RR activity over prolonged periods, confirming their stability. Among them, HR-Fe_2O_3 catalyst exhibits the highest NO_2RR performance, achieving an average NH_4^+ production rate of 153.0 nmol s^{-1} cm^{-2} and FE_{NH4+} of 93%, which is competitive with findings reported in the literature (**Table S3**). While NH_4^+ production rate and FE_{NH4+} are critical metrics for evaluating catalyst performance, the HR-Fe_2O_3 catalyst also excels in other key performance metrics.[89] Specifically, it demonstrates an exceptionally high partial current density for NH_4^+ production, reaching ~ 96.5 mA cm^{-2} at -1.0 V vs RHE, positioning it among the most active NO_2RR catalyst for NH_4^+ generation in literature (**Table S3**). While it is also important to evaluate NO_2RR performance at lower concentrations and in conditions representative of real wastewater (NO_x concentration ranging from 0.88 mM to 1.95 M),[99,100] the investigation extends to experiment with PAAE (plasma air activated electrolyte). This electrolyte solution is generated using a plasma system as discussed in previous works[6,44,81] (**Experimental Section**). Through this approach, it enables a decentralized, air-to-ammonia production pathway, independent of wastewater sources, thus broadening its applicability across a wide range of deployable scenarios. Building on previous studies, this work focuses on optimizing the production of NO_2^- over NO_3^- by manipulating various operating conditions. First, the pH of the reaction medium solution was altered: comparing neutral (deionized water) to alkaline conditions (0.1 M KOH). The results (**Figure S19a**) indicate that the alkaline condition (0.1 M KOH) significantly favors the production of NO_2^- (9.6 mM) over NO_3^- (0.8 mM), whereas in neutral environments, the production trends reverse, favoring NO_3^- over NO_2^-. Further, the production of NO_x via plasma was tested across different plasma voltages, as voltage is reported to fundamentally affect the concentration of NO_x production.[101,102] The results (**Figure S19b**) indicate that the highest amounts of NO_2^- and total NO_x are produced at 200 V,

with concentrations of 13.7 and 15.0 mM, respectively. NO_xRR performance testing in the optimally produced PAAE was conducted for 10 cycles (0.5 h chronoamperometry each cycle) within a commercial H-cell using pristine Fe_2O_3 and the best performing catalyst, HR-Fe_2O_3. The results further demonstrate the high stability of both Fe_2O_3 and HR-Fe_2O_3 across the 10-cycle operation at -1.0 V vs RHE, evidenced by steady chronoamperometric *i-t* curves and consistent NH_4^+ production rates (**Figure S20a** and **S20b**, respectively). Additionally, the results suggest that HR-Fe_2O_3 outperforms pristine Fe_2O_3 even under low NO_x concentrations, achieving a stable NH_4^+ production rate of 32.0 nmol s^{-1} cm^{-2} and a steady current density of ~ 52 mA cm^{-2} across 10-cycle tests at -1.0 V vs RHE. These results are comparable to those reported in the literature (**Table S3**) for studies involving similar low concentrations of NO_x. Hence, conducting NO_xRR using PAAE reveals the potential for a self-sustaining NH_4^+ production system through the integration of a plasma-electrolyzer setup. Furthermore, the ability of HR-Fe_2O_3 to efficiently convert trace amounts of NO_x to NH_4^+ in PAAE underscores its potential for real-world applications, particularly in treating waste streams from industries, power plants, and agriculture where NO_x is commonly found at low concentrations.

3 Conclusions

In conclusion, this work addresses the key knowledge gaps regarding the ERC-treated Fe-based catalysts with structural disorders in enhancing NO_2RR activity for NH_4^+ production in alkaline environments. A combination of *ex situ* and *in situ* characterization techniques collectively reveals that more negative ERC potentials enhance the reduction of surface Fe_2O_3 to FeO and metallic Fe, optimizing $Fe^{3+}/Fe^{2+}/Fe$ components, while simultaneously inducing significant lattice strain. This strain alters the d-band structure, promoting the hydrogenation of NO_2RR intermediates and enhancing NH_4^+ production. These findings underscore the synergistic effects of lattice strain engineering and $Fe^{3+}/Fe^{2+}/Fe$ components in creating highly effective active sites for NO_2RR, offering valuable insights for designing next-generation metal oxide catalysts. Additionally, this work addresses significant knowledge gaps in utilizing plasma technology to optimize NO_x feedstocks generation for NO_2^- formation. Systematic optimization of plasma conditions (solution pH and reactor voltage) enhances NO_2^- generation up to 13.7 mM, thereby offering a more efficient and targeted feedstock for NO_2RR. Overall, this work showcases the direct reduction of NO_2^- to NH_4^+ offers substantial advantages for green ammonia production, bypassing the most energy-intensive NO_3^--to-NO_2^- step and reducing overall energy costs. The enhanced hydrogenation capabilities of structurally engineered Fe_2O_3 catalysts in this work enables greater selectivity toward NH_4^+, with minimal H_2 by-products, thereby improving sustainability. Moreover, the integration of this plasma-electrolyzer system enables a decentralized, self-sustaining pathway for transforming air-derived NO_x into ammonia-related products on demand.

4 Experimental

View Article Online
DOI: 10.1039/D5TA09764A

4.1 Materials

All chemical reagents and solvents utilized in this work were used as received and without any further purification. Deionized water (resistivity 18.2 MΩ cm^{-1}) was used throughout all experiments.

4.2 Catalyst Synthesis

Fe_2O_3 catalyst powders were prepared through a precipitation method followed by calcination. First, 2 g of iron (III) nitrate nonahydrate (Sigma Aldrich, ≥ 99.95 %) was dissolved in 15 mL of deionized water and stirred for 0.5 h to achieve a homogeneous solution. This solution was then gradually added dropwise to 100 mL of a 1 mol L^{-1} Na_2CO_3 (Chem-Supply, analytical grade, 99.5 %) solution maintained at 60 °C. The mixture was aged and stirred continuously for 3 h. The resulting slurry was centrifuged and washed with ethanol (Chem-Supply, analytical grade, 99.5 %) and water (3 to 5 times each) to remove impurities, then dried overnight at 100 °C. The black crystals obtained were ground into powders and calcined in flowing air (Coregas, purity 100%) at 400 °C for 2 h, yielding brown Fe_2O_3 powders.

To prepare pristine Fe_2O_3 working electrodes, these Fe_2O_3 powders were spray-cast onto carbon fibre paper. Specifically, 3 mg of Fe_2O_3 powder was dispersed in a solution containing 1 mL deionized water, 1 mL ethanol, and 30 µL of a Nafion 117 solution (Sigma-Aldrich, ~ 5% in a mixture of lower aliphatic alcohols and water). The mixture was sonicated for 10 to 15 mins to ensure homogeneity. One-third of this mixture was sprayed onto carbon fibre paper placed on a hot plate at 110 °C, evenly covering an area of 1 cm × 6 cm. After cooling, the sprayed carbon fibre paper was cut into six pristine Fe_2O_3 electrodes.

To modify the surface properties of Fe_2O_3, ERC strategy was employed, with the ERC treated Fe_2O_3 electrodes referred to as eR-Fe_2O_3. Specifically, prior to electrochemical testing, the Fe_2O_3 electrodes were pre-treated at reduction potentials of -1.0 V and -2.0 V vs RHE for 0.5 h. The Fe_2O_3 electrodes conditioned at -1.0 V are referred to as Low-Reduction Fe_2O_3 (LR-Fe_2O_3), while those treated at -2.0 V are named as High-Reduction Fe_2O_3 (HR-Fe_2O_3). This pre-treatment was conducted in a commercial three-electrode H-cell containing 0.1 M KOH (Sigma Aldrich, ACS reagent grade, 90 % flakes) and 0.1 M KNO_2 (Sigma Aldrich, ACS reagent grade, ≥ 96.0 %) as the catholyte, similar to the setup used for electrochemical NO_2RR-to-NH_4^+ activity testing.

4.3 Electrochemical Experiments

All chemical reagents and solvents utilized in this work were used as received and without any further purification. Deionized water (resistivity 18.2 MΩ cm^{-1}) was used throughout all experiments. The electrocatalytic NO_2RR-to-NH_4^+ was carried out using a commercial H-cell setup. A three-electrode system was employed, comprising the eR-Fe_2O_3 catalyst as the working electrode (cathode), a Pt plate as the counter electrode (anode), and a Hg/HgO reference electrodes. The anolyte was 50 mL of 0.1 M KOH solution, whereas the catholyte was 50 mL

of 0.1 M KOH with 0.1 M KNO_2. An anion exchange membrane (AEM) (Dioxide Materials, X37-50 Grade RT) was used to separate the electrolytes while allowing ions to pass through. PAAE was also used as catholyte to evaluate the NO_2RR performance of the catalysts at lower concentrations and in conditions representative of real wastewater.[99,100] All electrochemical NO_2RR processes were performed using an Autolab Potentiostat (Nova 2 Metrohm).

Chronoamperometry tests were employed to identify the optimal potential for maximum NH_4^+ production efficiency. Each test was conducted for a duration of 15 mins and repeated three times to obtain average values. All potentials were converted to the RHE using the following equations:[103–105]

$$E_{RHE}\ (V) = E_{Hg/HgO}\ (V) + 0.098 + 0.059 \times pH$$

Long-term stability was assessed at the optimal applied potential under conditions similar to the chronoamperometry tests. The stability tests consisted of 15 cycles at the optimal potential, with each cycle lasting 30 mins. LSV measurements were conducted using the same H-cell setup under three different catholyte conditions: 0.1 M KOH, 0.1 M KOH + 0.1 M KNO_3, and 0.1 M KOH + 0.1 M KNO_2. EIS experiments were performed under similar conditions to the chronoamperometry tests, with a frequency range from 1 MHz to 0.01 Hz. The measurements were taken at potential of 0.615 V vs RHE.

The ECSAs of the catalysts were estimated using the CDL method. Briefly, cyclic voltammetry (CV) scans were recorded within a potential window of ± 0.05 V around each catalyst's onset potential, as identified from the LSV curves. The scan rates used were 100, 200, 300, 400, and 500 mV s^{-1}. The differences between the cathodic and anodic currents at the midpoint potential were plotted against the scan rates. The slope of the linear fit to this plot corresponds to the CDL. The ECSA was then calculated by dividing the CDL of the catalyst by the specific capacitance of a reference blank glassy carbon electrode (40 µF cm^{-2}) and multiplying by the geometric surface area of the electrode.[45]

4.4 Products Analysis

The main text of the article should appear here with headings as appropriate. The concentration of NH_4^+ produced in the catholyte was determined using the indophenol blue test. In this method, 0.5 mL of the catholyte sample was transferred into a 1.5 mL sample tube. To this, 0.4 mL of a 1 M NaOH solution (Sigma-Aldrich semiconductor grade, 99.99%) containing 5 wt.% salicylic acid (Sigma-Aldrich ACS grade, 99.0%) and 5 wt.% sodium citrate (Sigma-Aldrich ACS grade, 99.0%) was added, followed by 0.1 mL of a 0.05 M sodium hypochlorite solution (Sigma-Aldrich ACS grade, 10-15%) and 30 µL of a 1 wt.% sodium nitroferricyanide solution (Sigma-Aldrich ACS grade, 99 %). The mixture was thoroughly mixed and incubated in the dark at room temperature for 1 h. If the NH_4^+ concentration was excessively high, the catholyte was appropriately diluted prior to analysis. After incubation, the amount of NH_4^+ was quantified using ultraviolet-visible (UV-Vis) spectroscopy (Shimadzu, UV-360). Absorbance measurements were taken over wavelengths ranging from 550 to 800 nm. A calibration curve was constructed using the peak absorbance values (**Figure S21**). The performance of the catalysts in generating NH_4^+ was assessed by calculating the production rate ($Rate_{NH4+}$) and Faradaic efficiency (FE_{NH4+}) using the following equations:[106,107]

$$\text{Rate}_{\text{NH4+}} = \frac{[NH_4^+] \cdot V}{t \cdot S}$$

$$\text{FE}_{\text{NH4+}} = \frac{n \cdot F \cdot [NH_4^+] \cdot V}{Q}$$

where V is the volume of catholyte, t is time taken for NO_2RR, S is the effective area of working electrode, n is the desired electrons to synthesis one NH_4^+ molecule (n = 6), F is the Faraday constant (F = 96485.33 As mol^{-1}) and Q is the overall electrical energy consumed by electrodes throughout the duration of the electrochemical NO_2RR process.

In addition, ion chromatography (IC) was employed to quantify the concentrations of NH_4^+, NO_2^-, and NO_3^- and validate the calorimetric methods. The analyses were performed using an AQ400 ion chromatograph from Seal Analytical. To measure the amount of H_2 produced in the cathodic chamber, the solution was purged with Ar (Coregas, > 99.95% purity) gas for approximately 15 mins before conducting performance tests. A Shimadzu GC-2010 gas chromatography (GC) equipped with a thermal conductivity detector (TCD) and a Supelco Carboxen 1010 column was used for analysis. A calibration curve (**Figure S22**) was generated using known concentrations of H_2 to ensure accurate quantification.

4.5 Physical Characterization

For the study of surface morphology, crystal size, and surface element distribution of the catalysts, a Nano SEM 230 scanning electron microscope (SEM) and a FEI Tecnai G2 20 transmission electron microscope (TEM) were utilized. An accelerating voltage of 200 kV was applied for the TEM measurement. To prepare samples for TEM analysis, the catalyst nanoparticles were first scrapped off from the electrode substrate. They were then dispersed in ethanol by gentle ultrasonic agitation for a few minutes. Using a micropipette, a small droplet of the resulting dispersed suspension was drop-cast onto a gold TEM grid. Finally, the samples were dried under ambient conditions before being used for TEM measurement. X-ray diffraction (XRD) studies were performed using a XPERTPRO diffractometer with Cu Kα radiation (λ = 1.54060 Å). The scanning range spanned from 10° to 90° with a step size of 0.013°, aiming to identify the phase compositions and crystallinity of the catalysts. Data collected from the XRD experiments were analyzed using the Highscore Plus software.

The surface chemical states of the catalysts were investigated using a Thermo ESCALAB250Xi X-ray photoelectron spectrometer (XPS). A monochromatic Al Kα source with an excitation energy of 1486.68 eV was employed. The instrument operated at a typical power of 120 W, with an average spot size of 500 µm in diameter. Survey scans were recorded with a pass energy of 100 eV. While detailed regional scans used a pass energy of 20 eV. Calibration of the C 1s XPS spectra were performed by setting the graphitic C-C peak position to 284.8 eV. Raman spectra were acquired at room temperature using either an inVia 2 or an inVia Qontor Raman spectrometer. The inVia 2 instrument utilized a 532 nm wavelength diode laser

View Article Online
DOI: 10.1039/D5TA00764A

with 50 × magnification, while the inVia Qontor used a 514 nm diode laser, also at 50 × magnification. These measurements provided insights into the surface chemistry and composition of the catalysts. Additionally, *in situ* Raman measurements were conducted under applied potentials corresponding to the electrochemical reactions being studied, maintaining similar operational parameters.

In situ Fourier transform infrared (FTIR) measurements were performed at the infrared beamline of the Australian Synchrotron. The experimental setup involved a three-electrode electrochemical cell equipped with a ZnSe crystal serving as the infrared transmission window. An Ag/AgCl electrode acted as the reference electrode, while a Pt wire served as the counter electrode. The working electrode (i.e., pristine Fe_2O_3, LR-Fe_2O_3, and HR-Fe_2O_3) was connected to a potentiostat to apply the required potential for the electrochemical reaction under investigation. FTIR spectra were continuously collected during the experiments in reflection mode at a resolution of 4 cm^{-1}. To enhance the signal-to-noise ratio, each spectrum was the result of accumulating 512 scans. Background spectra were obtained using the same setup at open-circuit voltage before commencing the tests.

In situ Fe K-edge XANES measurement was carried out at the XAS beamline of the Australian Synchrotron Center. The Data were collected in fluorescence mode using a solid-state 18-element detector. The *in situ* cell was mounted on the beamline sample stage, with the electrode oriented at a 45° angle relative to the fluorescence detector.[108] The incident beam intensity was monitored using an OKEN ionization chamber, and all measurements were performed at ambient temperature.

In situ powder diffraction (PD) experiments were carried out using a custom-designed three-electrode electrochemical cell, equipped with a Kapton window (2 cm diameter) to enable X-ray irradiation.[109] For the measurements, the cell was configured with an Ag/AgCl electrode as the reference, a Pt wire as the counter electrode, and the prepared catalyst as the working electrode.

4.6 Plasma System for PAAE Generation

An in-house, custom-built plasma system (as described in the work by Jing et al.[6]), comprising of a plasma generator ('Leap 100' from PlasmaLeap Technologies) and a plasma reactor generating PAAE (plasma air activated electrolyte), was set up as illustrated in **Figure S23**. The plasma reactor was filled with 250 mL of 0.1 M KOH. Air (Coregas, purity 100%) was fed into the plasma system at a constant flowrate of 20 L/min. The plasma system reaction was operated under constant plasma generator operating parameters (i.e., voltage, duty, discharge frequency, and resonance frequency) for 2 h, with the solution in the reactor continuously stirred at constant speed of 350 rpm. After 2 h, the plasma activated solution, PAAE rich in NO_x species, including NO_2^- and NO_3^-, was cooled down to room temperature before being used for subsequent electrochemical measurements.

4.7 Computational Methods

All spin-polarized calculations were implemented using the Vienna Ab initio Simulation Package (VASP) with the Projector Augmented Wave (PAW) method, interfaced through the Atomic Simulation Environment (ASE). Electronic wavefunctions were expanded in a plane wave basis set with a 500 eV cutoff energy using gamma-point calculations. Electronic self-consistency was achieved with a convergence criterion of 10^{-6} eV, while ionic relaxations were terminated when forces on all unconstrained atoms fell below 0.05 eV/Å. The Perdew-Burke-Ernzerhof (PBE) functional was employed to account for exchange-correlation effects within the generalized gradient approximation (GGA) framework. To accurately account for the strongly correlated Fe 3d electrons, the DFT+U approach was implemented with a Hubbard U parameter of 4.2 eV for Fe atoms, following the Dudarev's formalism. To model hematite surfaces a five-layer α-Fe_2O_3(104) slab with a 15 Å vacuum gap in the z-direction was constructed (**Figure S24**). The top three atomic layers were fully relaxed to interact with adsorbates, while the bottom two layers were constrained to maintain bulk-like properties. The charged NO_2^- species was avoided as a reference in our DFT calculation. A thermodynamic cycle method was instead used to find the reference energy for NO_2^-. This approach uses the deprotonation of HNO_2 as a reference.

Conflicts of interest

There are no conflicts to declare.

Data availability

The data supporting this article have been included as part of the supplementary information (SI). Supplementary Information is available. See DOI: https://doi.org/xxx.

Acknowledgements

The work was supported by the Australian Research Council (ARC) Training Centre for Global Hydrogen Economy (IC200100023). The authors acknowledge research funding provided by the ARC (DE230100789 and DE230101396). R.D. acknowledges funding from UNSW Scientia Fellowship. Z. M. acknowledges UNSW-Tsinghua Collaborative Research Seed Program 2023 and the fellowship program by the International Hydrogen Research Collaboration Program funded by Commonwealth Scientific and Industrial Research Organisation (CSIRO). The authors also acknowledge the Infrared Microscopy/ANSTO Grant (AS241/IRM/21262) for the *in situ* FTIR beamtime, XAS/ANSTO Grant (AS261/XAS/24311a) for the *in situ/ ex situ* XANES, and PD/ANSTO Grant at the Australian Synchrotron

References

1 Eliseev, G. In *2024 Annual Conference (Fertecon/S&P Global Commodity Insights)*; S&P Global Commodity Insights (Fertecon): Conference Presentation, 2024; pp 1–17.

2 Wang, H.; Lin, N.; Arzumanyan, M. *Gases* **2024**, *4*, 224–235. https://doi.org/10.3390/gases4030013.

3 Wang, Y.; Zhou, W.; Jia, R.; Yu, Y.; Zhang, B. *Angew. Chemie Int. Ed.* **2020**, *59* (13), 5350–5354. https://doi.org/10.1002/anie.201915992.

4 Wang, Y.; Xu, A.; Wang, Z.; Huang, L.; Li, J.; Li, F.; Wicks, J.; Luo, M.; Nam, D.-H.; Tan, C.-S.; Ding, Y.; Wu, J.; Lum, Y.; Dinh, C.-T.; Sinton, D.; Zheng, G.; Sargent, E. H. *J. Am. Chem. Soc.* **2020**, *142* (12), 5702–5708. https://doi.org/10.1021/jacs.9b13347.

5 Guo, Y.; Zhang, R.; Zhang, S.; Zhao, Y.; Yang, Q.; Huang, Z.; Dong, B.; Zhi, C. *Energy Environ. Sci.* **2021**, *14* (7), 3938–3944. https://doi.org/10.1039/d1ee00806d.

6 Sun, J.; Alam, D.; Daiyan, R.; Masood, H.; Zhang, T.; Zhou, R.; Cullen, P. J.; Lovell, E. C.; Jalili, A.; Amal, R. *Energy Environ. Sci.* **2021**, *14* (2), 865–872. https://doi.org/10.1039/d0ee03769a.

7 Serpell, O.; Hsain, Z.; Chu, A.; Johnsen, W. *Ammonia's Role in a Net-Zero Hydrogen Economy*; 2023.

8 Daiyan, R.; Tran-Phu, T.; Kumar, P.; Iputera, K.; Tong, Z.; Leverett, J.; Khan, M. H. A.; Asghar Esmailpour, A.; Jalili, A.; Lim, M.; Tricoli, A.; Liu, R.-S.; Lu, X.; Lovell, E.; Amal, R. *Energy Environ. Sci.* **2021**, *14* (6), 3588–3598. https://doi.org/10.1039/d1ee00594d.

9 Smith, C.; Hill, A. K.; Torrente-Murciano, L. *Energy Environ. Sci.* **2020**, *13* (2), 331–344. https://doi.org/10.1039/c9ee02873k.

10 Ye, D.; Tsang, S. C. E. *Nat. Synth.* **2023**, *2* (7), 612–623. https://doi.org/10.1038/s44160-023-00321-7.

11 Carreon, M. L. *J. Phys. D. Appl. Phys.* **2019**, *52* (48), 483001. https://doi.org/10.1088/1361-6463/ab3b2c.

12 Bian, X.; Zhao, Y.; Zhang, S.; Li, D.; Shi, R.; Zhou, C.; Wu, L. Z.; Zhang, T. *ACS Mater. Lett.* **2021**, *3* (11), 1521–1527. https://doi.org/10.1021/ACSMATERIALSLETT.1C00504/SUPPL_FILE/TZ1C00504_SI_001.PDF.

13 Lin, B.; Wiesner, T.; Malmali, M. *ACS Sustain. Chem. Eng.* **2020**, *8* (41), 15517–15531. https://doi.org/10.1021/acssuschemeng.0c04313.

14 Hawtof, R.; Ghosh, S.; Guarr, E.; Xu, C.; Sankaran, R. M.; Renner, J. N. *Asian J. Chem.* **2019**, *31* (2), 5778–5789. https://doi.org/10.1126/sciadv.aat5778.

15 He, Y.; Chen, Z.; Li, Z.; Niu, G.; Tang, J. *Front. Optoelectron.* **2018**, *11* (1), 92–96. https://doi.org/10.1007/s12200-018-0807-z.

16 Giddey, S.; Badwal, S. P. S.; Munnings, C.; Dolan, M. *ACS Sustain. Chem. Eng.* **2017**, *5* (11), 10231–10239. https://doi.org/10.1021/acssuschemeng.7b02219.

17 Kumari, S.; Pishgar, S.; Schwarting, M. E.; Paxton, W. F.; Spurgeon, J. M. *Chem. Commun.* **2018**, *54* (95), 13347–13350. https://doi.org/10.1039/c8cc07869f.

18 Du, H. L.; Chatti, M.; Hodgetts, R. Y.; Cherepanov, P. V.; Nguyen, C. K.; Matuszek, K.; MacFarlane, D. R.; Simonov, A. N. *Nature* **2022**, *609* (7928), 722–727. https://doi.org/10.1038/s41586-022-05108-y.

19 Chen, H.; Yuan, D.; Wu, A.; Lin, X.; Li, X. *Waste Dispos. Sustain. Energy* **2021**, *3*, 201–217. https://doi.org/10.1007/s42768-021-00074-z.

20 Li, L.; Tang, C.; Cui, X.; Zheng, Y.; Wang, X.; Xu, H.; Zhang, S.; Shao, T.; Davey, K.; Qiao, S.-Z. *Angew. Chemie* **2021**, *133* (25), 14250–14256. https://doi.org/10.1002/anie.202104394.

21 Li, W.; Zhang, S.; Ding, J.; Liu, J.; Wang, Z.; Zhang, H.; Ding, J.; Chen, L.; Liang, C. *ACS Sustain. Chem. Eng.* **2023**, *11* (3), 1168–1177. https://doi.org/10.1021/acssuschemeng.2c06525.

22 Zhang, Z.; Zhang, N.; Zhang, J.; Deng, B.; Cao, Z.; Wang, Z.; Wei, G.; Zhang, Q.; Jia, R.; Xiang, P.; Xia, S. *Chem. Eng. J.* **2024**, *483*, 148952. https://doi.org/10.1016/j.cej.2024.148952.

23 Yin, S.; Cao, R.; Han, Y.; Shang, J.; Zhang, J.; Jiang, W.; Liu, G. *J. Energy Chem.* **2024**, *96*, 642–668. https://doi.org/10.1016/j.jechem.2024.05.023.

24 Zou, X.; Xie, J.; Wang, C.; Jiang, G.; Tang, K.; Chen, C. *Chinese Chem. Lett.* **2023**, *34* (6), 107908. https://doi.org/10.1016/j.cclet.2022.107908.

25 Fang, J.-Y.; Fan, J.-L.; Liu, S.-B.; Sun, S.-P.; Lou, Y.-Y. *Materials (Basel).* **2023**, *16* (11), 4000. https://doi.org/10.3390/ma16114000.

26 Xie, L.; Wang, Y.; Kong, Q.; Cao, R. *ChemCatChem* **2024**, *16* (21), e202400956. https://doi.org/10.1002/cctc.202400956.

27 Yu, Z.; Gu, M.; Wang, Y.; Li, H.; Chen, Y.; Wei, L. *Adv. Energy Sustain. Res.* **2024**, *5* (5), 2300284. https://doi.org/10.1002/aesr.202300284.

28 Liang, J.; Li, Z.; Zhang, L.; He, X.; Luo, Y.; Zheng, D.; Wang, Y.; Li, T.; Yan, H.; Ying, B.; Sun, S.; Liu, Q.; Hamdy, M. S.; Tang, B.; Sun, X. *Chem* **2023**, *9* (7), 1768–1827. https://doi.org/10.1016/j.chempr.2023.05.037.

29 Li, T.; Tang, C.; Guo, H.; Wu, H.; Duan, C.; Wang, H.; Zhang, F.; Cao, Y.; Yang, G.; Zhou, Y. *ACS Appl. Mater. Interfaces* **2022**, *14* (44), 49765–49773. https://doi.org/10.1021/acsami.2c14215.

30 Li, T.; Tang, C.; Guo, H.; Yang, J.; Zhang, F.; Yang, G.; Zhou, Y. *Chem. Eng. J.* **2024**, *485*, 149560. https://doi.org/10.1016/j.cej.2024.149560.

31 Liu, Q.; Liu, Q.; Xie, L.; Yue, L.; Li, T.; Luo, Y.; Li, N.; Tang, B.; Yu, L.; Sun, X. *Chem. Commun.* **2022**, *58* (33), 5160–5163. https://doi.org/10.1039/d2cc00611a.

32 Chen, G.-F.; Yuan, Y.; Jiang, H.; Ren, S.-Y.; Ding, L.-X.; Ma, L.; Wu, T.; Lu, J.; Wang, H. *Nat. Energy* **2020**, *5* (8), 605–613. https://doi.org/10.1038/s41560-020-0654-1.

33 Hou, Z.; Cui, C.; Li, Y.; Gao, Y.; Zhu, D.; Gu, Y.; Pan, G.; Zhu, Y.; Zhang, T. *Adv. Mater.* **2023**, *35* (39), 2209876. https://doi.org/10.1002/adma.202209876.

34 Herklotz, A.; Lee, D.; Guo, E. J.; Meyer, T. L.; Petrie, J. R.; Lee, H. N. *J. Phys. Condens. Matter* **2017**, *29* (49), 493001. https://doi.org/10.1088/1361-648X/aa949b.

35 Fang, L.; Wang, S.; Song, C.; Lu, S.; Yang, X.; Qi, X.; Liu, H. *Chem. Eng. J.* **2022**, *446*, 137341. https://doi.org/10.1016/j.cej.2022.137341.

36 Qin, Y.; Yu, T.; Deng, S.; Zhou, X.-Y.; Lin, D.; Zhang, Q.; Jin, Z.; Zhang, D.; He, Y.-B.; Qiu, H.-J.; He, L.; Kang, F.; Li, K.; Zhang, T.-Y. *Nat. Commun.* **2022**, *13* (1), 3784. https://doi.org/10.1038/s41467-022-31468-0.

37 Li, J.; Zhan, G.; Yang, J.; Quan, F.; Mao, C.; Liu, Y.; Wang, B.; Lei, F.; Li, L.; Chan, A. W. M.; Xu, L.; Shi, Y.; Du, Y.; Hao, W.; Wong, P. K.; Wang, J.; Dou, S.-X.; Zhang, L.; Yu, J. C. *J. Am. Chem. Soc.* **2020**, *142* (15), 7036–7046. https://doi.org/10.1021/jacs.0c00418.

38 Liu, S.; Miao, W.; Ma, K.; Teng, H.; Zhang, X.; Li, J.; Li, W.; Cui, X.; Jiang, L. *Appl. Catal. B Environ. Energy* **2024**, *350*, 123919. https://doi.org/10.1016/j.apcatb.2024.123919.

39 Wu, J.; Yu, Y.-X. *Catal. Sci. Technol.* **2021**, *11* (21), 7160–7170. https://doi.org/10.1039/d1cy01217g.

40 Zhang, X.; Zhang, Q.; Peng, Y.; Ma, X.; Fan, G. *Int. J. Hydrogen Energy* **2022**, *47* (12), 7793–7801. https://doi.org/10.1016/j.ijhydene.2021.12.122.

41 Chen, F.-Y.; Wu, Z.-Y.; Gupta, S.; Rivera, D. J.; Lambeets, S. V.; Pecaut, S.; Kim, J. Y. T.; Zhu, P.; Finfrock, Y. Z.; Meira, D. M.; King, G.; Gao, G.; Xu, W.; Cullen, D. A.; Zhou, H.; Han, Y.; Perea, D. E.; Muhich, C. L.; Wang, H. *Nat. Nanotechnol.* **2022**, *17* (7), 759–767. https://doi.org/10.1038/s41565-022-01121-4.

42 Duan, T.; Chen, Y.; Wen, Q.; Duan, Y. *RSC Adv.* **2015**, *5* (25), 19601–19612. https://doi.org/10.1039/c5ra01876e.

43 Rajaramanan, T.; Natarajan, M.; Ravirajan, P.; Senthilnanthanan, M.; Velauthapillai, D. Ruthenium (Ru) *Energies* **2020**, *13* (7), 1532. https://doi.org/10.3390/en13071532.

44 Lim, M.; Ma, Z.; O'Connell, G.; Yuwono, J. A.; Kumar, P.; Jalili, R.; Amal, R.; Daiyan, R.; Lovell, E. C. *Small* **2024**, *20* (33), 2401333. https://doi.org/10.1002/smll.202401333.

45 Ma, Z.; Tsounis, C.; Toe, C. Y.; Kumar, P. V.; Subhash, B.; Xi, S.; Yang, H. Y.; Zhou, S.; Lin, Z.; Wu, K. H.; Wong, R. J.; Thomsen, L.; Bedford, N. M.; Lu, X.; Ng, Y. H.; Han, Z.; Amal, R. *ACS Catal.*

2022, *12* (9), 4792–4805. https://doi.org/10.1021/acscatal.1c05431.
46 Li, P. X.; Qu, L.-M.; Zhang, C.-H.; Ren, X.-B.; Wang, H.-X.; Zhang, J.-L.; Mu, Y.-W.; Lü, B.-L. *J. Fuel Chem. Technol.* **2021**, *49* (10), 1558–1566. https://doi.org/10.1016/S1872-5813(21)60154-8.
47 Chen, H.; Ma, Y.; Han, Y.; Mao, X.; Hu, Y.; Zhao, X.; Dong, Q.; Wen, B.; Du, A.; Wang, X.; Lyu, X.; Jia, Y. *Small* **2024**, *20* (26), 2309689. https://doi.org/10.1002/smll.202309689.
48 Fu, Y. Y.; Wang, R. M.; Xu, J.; Chen, J.; Yan, Y.; Narlikar, A. V.; Zhang, H. *Chem. Phys. Lett.* **2003**, *379* (3–4), 373–379. https://doi.org/10.1016/j.cplett.2003.08.061.
49 Morgan, D. J. *X-Ray Photoelectron Spectroscopy (XPS): An Introduction*; 2014. http://sites.cardiff.ac.uk/xpsaccess/files/2014/07/AccessXPS_Primer_Paper.pdf.
50 Liang, X.; Wang, X.; Zhang, X.; Lin, S.; Ji, M.; Liu, Q.; Wang, M. *ACS Catal.* **2024**, *14* (7), 4648–4655. https://doi.org/10.1021/acscatal.4c00016.
51 Liu, C.; Zhang, G.; Zhang, W.; Gu, Z.; Zhu, G. *Proc. Natl. Acad. Sci.* **2023**, *120* (3), e2209979120. https://doi.org/10.1073/pnas.
52 Frankcombe, T. J.; Liu, Y. *Chem. Mater.* **2023**, *35* (14), 5468–5474. https://doi.org/10.1021/acs.chemmater.3c00801.
53 Biesinger, M. C.; Payne, B. P.; Grosvenor, A. P.; Lau, L. W. M.; Gerson, A. R.; Smart, R. S. C. *Appl. Surf. Sci.* **2011**, *257* (7), 2717–2730. https://doi.org/10.1016/j.apsusc.2010.10.051.
54 Bernal Romero, J.; Chavez, O.; Rodriguez, C.; Gonzalez, S.; Fregoso, J.; Carbajal, V.; Clavel, G.; Hudak, O.; Cheng, J.; Tandoc, J.; Brown, J.; Gao, L. *MRS Adv.* **2024**, *9* (15), 1176–1182. https://doi.org/10.1557/s43580-024-00866-5.
55 Rahul, R.; Singh, R. K.; Bera, B.; Devivaraprasad, R.; Neergat, M. *Phys. Chem. Chem. Phys.* **2015**, *17* (23), 15146–15155. https://doi.org/10.1039/c5cp00692a.
56 Antunes, V. G.; Figueroa, C. A.; Alvarez, F. *Langmuir* **2022**, *38* (6), 2109–2116. https://doi.org/10.1021/acs.langmuir.1c03189.
57 Kim, Y.; Watanabe, M.; Matsuda, J.; Song, J. T.; Takagaki, A.; Staykov, A.; Ishihara, T. *Appl. Catal. B Environ.* **2020**, *278*, 119292. https://doi.org/10.1016/j.apcatb.2020.119292.
58 Nasiri-Tabrizi, B. *J. Adv. Ceram.* **2014**, *3* (1), 31–42. https://doi.org/10.1007/s40145-014-0090-4.
59 Craciun, F.; Galassi, C.; Birjega, R. *J. Appl. Phys.* **2012**, *112* (12). https://doi.org/10.1063/1.4770326.
60 Li, J.; Wu, X. L.; Hu, D. S.; Yang, Y. M.; Qiu, T.; Shen, J. C. *Solid State Commun.* **2004**, *131* (1), 21–25. https://doi.org/10.1016/j.ssc.2004.04.026.
61 Perenlei, G.; Talbot, P. C.; Martens, W. N.; Riches, J.; Alarco, J. A. *RSC Adv.* **2017**, *7* (26), 15632–15643. https://doi.org/10.1039/c6ra27633d.
62 Sun, Y.; Ren, Y.; Liu, Y.; Wen, J.; Okasinski, J. S.; Miller, D. J. *Nat. Commun.* **2012**, *3*, 6–11. https://doi.org/10.1038/ncomms1963.
63 Lei, Q.; Huang, L.; Yin, J.; Davaasuren, B.; Yuan, Y.; Dong, X.; Wu, Z. P.; Wang, X.; Yao, K. X.; Lu, X.; Han, Y. *Nat. Commun.* **2022**, *13* (1), 4857. https://doi.org/10.1038/s41467-022-32601-9.
64 Fan, Q.; Yan, P.; Liu, F.; Xu, Z.; Liang, P.; Cao, X.; Ye, C.; Liu, M.; Zhao, L.; Ren, S.; Miao, H.; Zhang, X.; Yang, Z.; Ding, X.; Yang, J.; Kong, C.; Wu, Y. *Sci. Bull.* **2024**, *69* (18), 2881–2891. https://doi.org/10.1016/j.scib.2024.06.031.
65 Zaza, F.; Orio, G.; Serra, E.; Caprioli, F.; Pasquali, M. In *AIP Conference Proceedings*; 2015; Vol. 1667, p 1. https://doi.org/10.1063/1.4922560.
66 Biswas, M.; Misra, D.; Kundu, T. K. *Eur. Phys. J. B* **2023**, *96* (6), 74. https://doi.org/10.1140/epjb/s10051-023-00547-6.
67 Duan, J.; Zhao, Y.; Wu, Y.; Liu, Y.; Chen, J.; Yang, R.; Huang, J.; Luo, C.; Wu, M.; Zheng, X.; Li, P.; Jiang, X.; Guan, J.; Zhai, T. *Chem. Sci.* **2024**, *15*, 19546–19555. https://doi.org/10.1039/d4sc05873a.
68 Wen, W.; Yan, P.; Sun, W.; Zhou, Y.; Yu, X.-Y. *Adv. Funct. Mater.* **2023**, *33* (6), 2212236. https://doi.org/10.1002/adfm.202212236.
69 Zhang, R.; Shang, S.; Wang, F.; Chu, K. *Dalt. Trans.* **2024**, *53* (8), 3470–3475. https://doi.org/10.1039/d4dt00043a.
70 Huang, K.; Tang, K.; Wang, M.; Wang, Y.; Jiang, T.; Wu, M. *Adv. Funct. Mater.* **2024**, *34* (24), 2315324. https://doi.org/10.1002/adfm.202315324.
71 Geng, J.; Ji, S. *Nano Res.* **2024**, *17* (6), 4898–4907. https://doi.org/10.1007/s12274-024-6480-1.
72 Zhao, C.; Tan, G.; Yang, W.; Xu, C.; Liu, T.; Su, Y.; Ren, H.; Xia, A. *Sci. Rep.* **2016**, *6* (1), 38603. https://doi.org/10.1038/srep38603.
73 Platt, P.; Mella, R.; DeMaio, W.; Preuss, M.; Wenman, M. R. *Comput. Mater. Sci.* **2017**, *140*, 322–333. https://doi.org/10.1016/j.commatsci.2017.09.001.
74 Cao, H.; Wang, G.; Zhang, L.; Liang, Y.; Zhang, S.; Zhang, X. *ChemPhysChem* **2006**, *7* (9), 1897–1901. https://doi.org/10.1002/cphc.200600130.
75 Chourpa, I.; Douziech-Eyrolles, L.; Ngaboni-Okassa, L.; Fouquenet, J. F.; Cohen-Jonathan, S.; Soucé, M.; Marchais, H.; Dubois, P. *Analyst* **2005**, *130* (10), 1395–1403. https://doi.org/10.1039/b419004a.
76 Phu, N. D.; Ngo, D. T.; Hoang, L. H.; Luong, N. H.; Chau, N.; Hai, N. H. *J. Phys. D. Appl. Phys.* **2011**, *44* (34). https://doi.org/10.1088/0022-3727/44/34/345002.
77 De Faria, D. L. A.; Venâncio Silva, S.; De Oliveira, M. T. *J. Raman Spectrosc.* **1997**, *28* (11), 873–878. https://doi.org/10.1002/(sici)1097-4555(199711)28:11<873::aid-jrs177>3.0.co;2-b.
78 Bhalerao, G. M.; Singh, M. K.; Sinha, A. K.; Ghosh, H. *Phys. Rev. B - Condens. Matter Mater. Phys.* **2012**, *86* (12), 125419. https://doi.org/10.1103/PhysRevB.86.125419.
79 Davydov, S. Y.; Posrednik, O. V. *Phys. Solid State* **2021**, *63* (4), 530–533. https://doi.org/10.1134/S1063783421040053.
80 Xiang, H.; Liu, W.; Su, L.; Chen, S.; Han, Y.; Zhu, C.; Wang, S.; Tan, C.; Zhang, L. *Sep. Purif. Technol.* **2024**, *330*, 125357. https://doi.org/10.1016/j.seppur.2023.125357.
81 Lim, M.; Sun, J.; Ma, Z.; Jalili, R.; Daiyan, R.; Lovell, E. C.; Amal, R. *ACS Appl. Nano Mater.* **2023**, *6* (6), 4936–4945. https://doi.org/10.1021/acsanm.3c00681.
82 Zhu, M. K.; Lu, P. X.; Hou, Y. D.; Song, X. M.; Wang, H.; Yan, H. *J. Am. Ceram. Soc.* **2006**, *89* (12), 3739–3744. https://doi.org/10.1111/j.1551-2916.2006.01281.x.
83 Yuan, Z.; Sohn, H. Y. *ISIJ Int.* **2014**, *54* (6), 1235–1243. https://doi.org/10.2355/isijinternational.54.1235.
84 Fu, W.; Hu, Z.; Zheng, Y.; Su, P.; Zhang, Q.; Jiao, Y.; Zhou, M. *Chem. Eng. J.* **2022**, *433*, 133680. https://doi.org/10.1016/j.cej.2021.133680.
85 Fang, J.-Y.; Zheng, Q.-Z.; Lou, Y.-Y.; Zhao, K.-M.; Hu, S.-N.; Li, G.; Akdim, O.; Huang, X.-Y.; Sun, S.-G. *Nat. Commun.* **2022**, *13* (1), 7899. https://doi.org/10.1038/s41467-022-35533-6.
86 Chu, K.; Luo, Y.; Shen, P.; Li, X.; Li, Q.; Guo, Y. *Adv. Energy Mater.* **2022**, *12* (3), 2103022. https://doi.org/10.1002/aenm.202103022.
87 Barbosa, A. I.; Costa Lima, S. A.; Reis, S. *Molecules* **2019**, *24* (2), 346. https://doi.org/10.3390/molecules24020346.
88 Al-Abduly, A.; Christensen, P. *Plasma Sources Sci. Technol.* **2015**, *24* (6), 065006. https://doi.org/10.1088/0963-0252/24/6/065006.
89 Han, S.; Li, H.; Li, T.; Chen, F.; Yang, R.; Yu, Y.; Zhang, B. *Nat. Catal.* **2023**, *6* (5), 402–414. https://doi.org/10.1038/s41929-023-00951-2.
90 Alenazi, N.; Hussein, M.; Alamry, K.; Asiri, A. A Real Sample Analysis. *J. Carbon Res.* **2018**, *4* (2), 30. https://doi.org/10.3390/c4020030.

91 Karelin, A. I.; Kayumov, R. R.; Dobrovolsky, Y. A. *Spectrochim. Acta Part A Mol. Biomol. Spectrosc.* **2019**, *215*, 381–388. https://doi.org/10.1016/j.saa.2019.03.007.

92 Verma, S. K.; Deb, M. K. *Anal. Chim. Acta* **2007**, *582* (2), 382–389. https://doi.org/10.1016/j.aca.2006.09.020.

93 Søndergaard, T.; Cleemann, L. N.; Zhong, L.; Becker, H.; Steenberg, T.; Hjuler, H. A.; Seerup, L.; Li, Q.; Jensen, J. O. *Electrocatalysis* **2018**, *9* (3), 302–313. https://doi.org/10.1007/s12678-017-0427-1.

94 Katipamula, S.; White, N. M.; Waldie, K. M. *Chem Catal.* **2023**, *3* (3), 100561. https://doi.org/10.1016/j.checat.2023.100561.

95 Zhang, X.; Liu, X.; Huang, Z.-F.; Guo, L.; Gan, L.; Zhang, S.; Ajmal, M.; Pan, L.; Shi, C.; Zhang, X.; Yang, G.; Zou, J.-*JACS Catal.* **2023**, *13* (22), 14670–14679. https://doi.org/10.1021/acscatal.3c04541.

96 Murphy, E.; Sun, B.; Rüscher, M.; Liu, Y.; Zang, W.; Guo, S.; Chen, Y. H.; Hejral, U.; Huang, Y.; Ly, A.; Zenyuk, I. V.; Pan, X.; Timoshenko, J.; Cuenya, B. R.; Spoerke, E. D.; Atanassov, P. *Adv. Mater.* **2024**, *36* (27), 2401133. https://doi.org/10.1002/adma.202401133.

97 Wang, Y.; Xia, S.; Cai, R.; Zhang, J.; Wang, J.; Yu, C.; Cui, J.; Zhang, Y.; Wu, J.; Yang, S.; Tan, H. H.; Wu, Y. *Small* **2023**, *19* (26), 2302295. https://doi.org/10.1002/smll.202302295.

98 Choi, S. R.; Lim, M.; Kim, D. Y.; An, W. Y.; Lee, S. W.; Choi, S.; Bae, S. J.; Yim, S. D.; Park, J. Y. *Int. J. Hydrogen Energy* **2022**, *47* (39), 17379–17392. https://doi.org/10.1016/j.ijhydene.2022.03.222.

99 Luo, W.; Guo, Z.; Ye, L.; Wu, S.; Jiang, Y.; Xu, P.; Wang, H.; Qian, J.; Zhou, X.; Tang, H.; Ge, Y.; Guan, J.; Yang, Z.; Nie, H. *Small* **2024**, *20* (30), 2311336. https://doi.org/10.1002/smll.202311336.

100 Li, Y.; Wang, C.; Yang, L.; Ge, W.; Shen, J.; Zhu, Y.; Li, C. *Adv. Energy Mater.* **2024**, *14* (7), 2303863. https://doi.org/10.1002/aenm.202303863.

101 Penetrante, B. M.; Hsiao, M. C.; Merritt, B. T.; Vogtlin, G. E. 1997; Vol. 106. https://doi.org/10.4271/971715.

102 McLarnon, C. R.; Penetrante, B. M. 1998. https://doi.org/10.4271/982434.

103 Ding, Z.; Wang, K.; Mai, Z.; He, G.; Liu, Z.; Tang, Z. *Int. J. Hydrogen Energy* **2019**, *44* (45), 24680–24689. https://doi.org/10.1016/j.ijhydene.2019.07.244.

104 Wang, M.; Ji, S.; Wang, H.; Wang, X.; Linkov, V.; Ma, X.; Wang, R. *J. Alloys Compd.* **2023**, *948*, 169713. https://doi.org/10.1016/j.jallcom.2023.169713.

105 Wang, H.; Wang, M.; Wang, J. *Curr. Chinese Sci.* **2023**, *3* (3), 204–212. https://doi.org/10.2174/2210298103666221102092735.

106 Lei, F.; Li, K.; Yang, M.; Yu, J.; Xu, M.; Zhang, Y.; Xie, J.; Hao, P.; Cui, G.; Tang, B. *Inorg. Chem. Front.* **2022**, *9* (11), 2734–2740. https://doi.org/10.1039/d2qi00489e.

107 Fan, X.; Zhao, D.; Deng, Z.; Zhang, L.; Li, J.; Li, Z.; Sun, S.; Luo, Y.; Zheng, D.; Wang, Y.; Ying, B.; Zhang, J.; Alshehri, A. A.; Lin, Y.; Tang, C.; Sun, X.; Zheng, Y. *Small* **2023**, *19* (17), 2208036. https://doi.org/10.1002/smll.202208036.

108 Ramadhany, P.; Trần-Phú, T.; Yuwono, J.A.; Hocking, R.K.; Ma, Z.; Ta, X.M.C.; Kumar, P.; Gunawan, D.; Johannessen, B.; Tricoli, A.; Simonov, A.N.; Amal, R.; Daiyan. R.; *Nat. Commun.* **2026,** 17, 1776. https://www.nature.com/articles/s41467-026-68481-6

109 Ma, Z.; Leverett, J.; Yuwono, J. A.; Pan, J.; Zhou, S.; Zhang, D.; Zhang, M.; Xie, B.; Peng, L.; Khan, M. H. A.; Londono, S. L.; Kumar, Priyank V.K.; Lovell, E.; Daiyan, R.; Amal, R. *Chem. Eng. J.* **2025***, 524, 168996.* https://doi.org/10.1016/j.cej.2025.168996

110 Blöchl, P. E. *Phys. Rev. B* **1994**, *50* (24), 17953–17979. https://doi.org/10.1103/PhysRevB.50.17953.

111 Kresse, G.; Joubert, D. *Phys. Rev. B* **1999**, *59* (3), 1758–1775. https://doi.org/10.1103/PhysRevB.59.1758.

112 Kresse, G.; Furthmüller, J. *Phys. Rev. B* **1996**, *54* (16), 11169–11186. https://doi.org/10.1103/PhysRevB.54.11169.

113 Kresse, G.; Furthmüller, J. *Comput. Mater. Sci.* **1996**, *6* (1), 15–50. https://doi.org/10.1016/0927-0256(96)00008-0.

114 Perdew, J. P.; Burke, K.; Ernzerhof, M. *Phys. Rev. Lett.* **1996**, *77* (18), 3865–3868. https://doi.org/10.1103/PhysRevLett.77.3865.

115 Cardenas-Flechas, L. J.; Barba-Ortega, J. J.; Joya, M. R. *Ceramica* **2022**, *68* (385), 52–59. https://doi.org/10.1590/0366-69132022683853152.

The data supporting this article have been included as part of the Supplementary Information. Supplementary information: Figures S1-S24 and Tables S1-S3. See DOI: [URL – format https://doi.org/DOI]

View Article Online
DOI: 10.1039/D5TA09764A